Green Chemistry

Accepted Manuscript

ROYAL SOCIETY OF CHEMISTRY

www.rsc.org/greenchem

Journal Name

ARTICLE

Received 00th January 20xx,

Accepted 00th January 20xx

DOI: 10.1039/x0xx00000x

www.rsc.org/

Sputtering processed highly efficient $Cu_2ZnSn(S,Se)_4$ solar cells by a low-cost, simple, environmentally friendly, and up-scalable strategy

Myeng Gil Gang[a,·], Seung Wook Shin[b,·,·] Chang Woo Hong[a], K.V. Gurav[a], Jihye Gwak[c], Jae HoYun[c], Jeong Yong Lee[b,*] and Jin Hyeok Kim[a,**]

Earth abundant copper-zinc-tin chalcogenide (CZTSSe) is an emerging material for the development of low cost and sustainable thin film solar cells (TFSCs). A low cost, green, and up-scalable approach to the fabrication of TFSCs through the sputtering process is main challenge to achieve high efficiency for $Cu_2ZnSn(S,Se)_4$ (CZTSSe) solar cells for industrialization. Based on a closed isothermal chamber annealing system, we could precisely calculate and control the chalcogenide partial vapour pressure during annealing process. We designed, developed, and optimized an environmentally friendly strategy to synthesis a high quality CZTSSe absorber thin film and to fabricate a solar cell without using toxic H_2Se and H_2S gases as the Se and S sources or any other volatile compounds (SnS and Sn), and chalcogenide diffusion barrier layer. We fabricated a CZTSSe TFSC with 9.24 % efficiency, which is the highest performance for sputtering processed CZTSSe TFSC prepared without using toxic gases and additional processes. Based on this green strategy, we also fabricated the integrated submodule using CZTSSe absorber layers with efficiencies as high as η = 2.76 % with eight interconnected cells (active area of 22.4 cm^2). Our studies on this green synthesis strategy for CZTSSe solar cells could introduce a possible path way to green fabrication for the low cost and highly efficient TFSC industrialization field.

Broader context

Kesterite $Cu_2ZnSn(S,Se)_4$ (CZTSSe) has emerged as a promising candidate for scalable photovoltaic applications due to its earth abundant elements, optical characteristics, and chemical stability. Currently, the highest recorded efficiency of kesterite CZTSSe thin film solar cells (TFSCs) is 12.7 % using a hybrid solution based process that involves the use of a toxic hydrazine hydrate solvent. Sputtering-based techniques yield a lower efficiency of 9.7 % for the CZTSSe absorber layer via the selenization of the sputtered precursor under a toxic H_2Se gas and Sn based vapour atmosphere. Although higher efficiencies were achieved by the above-mentioned techniques, the use of toxic processes in kesterite thin films significantly impeded photovoltaic industrialization. In this study, we report a simple, environmentally benign, eco-friendly sulfo-selenization route to produce a CZTSSe absorber for a TFSC with 9.24 % efficiency. The efficiency values reported in this study represent the highest solar cell performance for a device produced using the sputtering technique, without the use of toxic H_2Se gas, and additional processes. Our non-toxic approach for the fabrication of the kesterite CZTSSe absorber and high efficiency TFSCs represents the first step towards low-cost and large-area TFSC industrialization.

[a] Optoelectronic Convergence Research Center, Department of Materials Science and Engineering Chonnam Nation University, 300 YongBongDong, Puk-Gu, Gwangju 500-757 [b] Center for Namomaterials and Chemical Reactions, Institute for Basic Science, Daejeon 305-701, Korea [c] Photovoltaic Laboratory, Korea Institute of Energy Research, 71-2 Jang-Dong Yuseong-Gu, Daejeon 305-343, South Korea
[·] M.G. Gang and S.W. Shin contributed equally to this work [·,·] Present address: Department of Chemical Engineering and Materials Science, University of Minnesota, Minneapolis, Minnesota 55455, USA

Electronic Supplementary Information (ESI) available: [Experimental details, additional characterization data, and certificated conversion efficiency data]. See DOI: 10.1039/x0xx00000x

Journal Name

ARTICLE

Introduction

The semiconductor $Cu_2ZnSn(S,Se)_4$ (CZTSSe) containing earth abundant elements is an attractive candidate for light absorbing materials for low cost and highly efficient thin film solar cells (TFSCs) due to their outstanding optical characteristics and high theoretical efficiency.[1, 2] The reported studies over last several years of CZTSSe-based TFSCs have been adopted from that of $Cu(In,Ga)Se_2$ (CIGS) because of the similarity to the optical characteristics and structure of TFSCs.[3] With their outstanding characteristics and the many research efforts devoted to them, solar cells based on CZTSSe compounds showed rapid improvements and reached efficiencies up to 12.7 %[4], however, the device efficiencies are still far behind those of commercialized absorber materials such as CIGS (η = 21.7 %)[5] and CdTe (η = 19.6 %).[6]

Several synthetic techniques including vacuum and non-vacuum methods, were reported in the literature for the CZTSSe absorber layers.[1,7, 8] The highest power conversion efficiency (PCE) of 12.7 % for CZTSSe TFSCs was obtained using a hydrazine based solution process approach.[4] Although the performance of CZTSSe TFSCs adapting the hydrazine based hybrid slurry approach has been reported to be the highest, the hazards associated with highly toxic and explosive hydrazine may inhibit adaption of this technique.[9] More classical deposition methods were studied for easy transferability to industrial applications.[10, 11] In particular, the magnetron sputtering and co-evaporation processes were particularly successful and have shown comparable efficiencies.[3] Repins et al. have reported a 9.15 % efficient CZTSe solar cell using the CZTSe absorber prepared by a single step co-evaporation process.[12] With careful control of deposition rates and substrate temperature, Repins et al. successfully controlled the evaporation of volatile phases and prepared phase pure CZTSe films.[12] The 8.9% and 11.6 % efficient CZTSe TFSCs prepared by the selenization of a co-evaporated Cu-Zn-Sn-S containg precursor on thin TiN diffusion barrier/Mo coated soda lime glass at 590 ºC on a hot plate under an excess Se + N_2 atmosphere have been reported by Shin and Lee et al.[10, 13] Recently, Brammertz et al. have achieved a CZTSe TFSC with 9.7 % efficiency by the sputtering of Cu, Zn, and Cu_1Sn_9 layers followed by selenization using toxic H_2Se gas at 460 ºC for 15 min.[14] The adhesion issue of the metallic Cu_1Sn_9 layer in contact with Mo during the selenization process resulted in the formation of voids at the Mo /CZTS interface.[14] Although these studies have achieved high efficiency using CZTSSe absorber layers, the fabrication process is limited for commercial use of the emerging CZTSSe-based technologies due to the use of a toxic H_2Se gas (sputtering) or the lack of large area uniformity (co-evaporation). Considering the issues with these processes, the best fabrication route for CZTSSe is a two-step method, which should involve the sequential deposition of high-purity sputtered Cu, Zn and Sn from elemental targets followed by annealing at high temperatures using less toxic Se pellets instead of toxic H_2Se gas. It is very important to control the thickness and morphology of each metallic layer in the two-step process because these two factors eventually control the composition and morphology of the CZTSSe absorber layer after the annealing process. However, the CZTSSe TFSCs prepared using the two-step fabrication process suffered poor performances due to (i) the formation of many voids and unexpected phases between the Mo and CZTSSe layers and (ii) the $Mo(S,Se)_2$ interfacial layer with that was too thick (over 500 nm), during the annealing process under high vapour pressures of chalcogenide materials.[15,16, 17]

Normally, the formation of voids and, unexpected phases, as well as the increased instability near the back contact region, are closely related to the Sn loss from the kesterite CZTSSe thin films during the annealing process.[16-18] This Sn loss behaviour from the kesterite CZTSSe thin film is attributed to the instability of the Sn (IV) element, which is the particular chemistry of multivalent Sn during the annealing process.[16] The oxidation state of the multivalent Sn is determined by the partial pressure of the chalcogenide materials and the annealing temperature.[16] The oxidation state of Sn (II) is favoured, and the Sn(II) based compound is easily formed and vaporized at high annealing temperatures, low vapour pressures of the chalcogenide materials and open annealing atmosphere (Particularly, Ar or N_2 gases flow during annealing process).[16,17] This unusual chemistry of multivalent Sn in the kesterite thin films is the driving force for CZTS decomposition at the surface and back contact regions.[16] This detrimental effect worsens when the CZTSSe thin films are prepared by sulfurization or selenization in the open annealing system, indicating the uncontrollable chalcogenide vapour composition and pressure.[2] To prevent Sn loss from the kesterite thin film during annealing, research groups developed the annealing process under an atmosphere comprised of chalcogenide and Sn-containing materials.[19]

Conversely, the Mo back contact region reacts with the chalcogenide to form the $Mo(S,Se)_2$ interfacial layer, whose

thickness mainly depends on the vapour pressures of the chalcogenide materials.[10] They facilitate the formation of the Ohmic contact between the Mo and CZTSe layers of approximately one hundred manometer, while they adversely affects the poor performances under the thicker thickness of the $Mo(S,Se)_2$ interfacial layer.[10,16] This behaviour implied that the vapour pressure of the chalcogenide materials should be precisely controlled to achieve the high performance device.[16] Recently, the device performance could be effectively improved by introducing thin Se diffusion barrier layers such as TiN, TiB_2, Ag, and i-ZnO between the precursor and the Mo layer[10, 19-21] The enhanced device performances are attributed to the reduction of the series resistance (R_s) from the thinner $Mo(S,Se)_2$ interfacial layer and the improvement of the open circuit voltage (V_{oc}) from the improved stability in the back contact region and the reduction of unexpected phases. However, these additional processes including Sn-based compounds and the Se diffusion barrier layer in the fabrication of CZTSSe TFSCs might lead to significant limitations for industrial uses of the photovoltaic device. These issues clearly suggested that a new scientific approach is required that, can control the Sn loss and the thickness of the $Mo(S,Se)_2$ interfacial layer during the annealing process to form the high quality kesterite thin films. Recently, a possible solution for these difficulties in the CZTSSe TFSC was reported by Li et al.[22] They demonstrated the controllable thickness of $MoSe_2$ in the CZTSe absorber layer through an alloying process for the metallic precursor (called soft annealing), which acts as a temporary Se diffusion barrier, resulting in the fabrication of the 8.7 % efficient CZTSe TFSC.[22] One possibility for the fabrication of highly efficient CZTSSe TFSCs without using additional barrier layers has been suggested by introducing a soft-annealing step in the metallic precursor preparation and by precisely controlling the vapour pressures of the chalcogenide materials in the annealing process.

In this study, we report the kesterite CZTSSe TFSCs prepared by the sputtering technique and demonstrate a PCE of 9.24 %, which is the highest recorded efficiency for CZTSSe films prepared without using a toxic H_2Se gas. An important feature of this research is that the annealing process is conducted in a closed isothermal chamber system, and a green synthesis strategy is used to prepare the high quality CZTSSe absorber layer without using a toxic gas, any other volatile compounds, and a Se diffusion barrier layer on the precursor. This annealing system is expected to reach equilibrium without loss of Sn, and the vapour pressures of the chalcogenide materials can be precisely controlled in the reaction chamber during the annealing process. Based on this annealing system, we could precisely calculate the chalcogenide partial vapour pressure during annealing systems using study on chalcogenide species chemistry (See Fig.1). Thus, we systematically designed, developed, and optimized the CZTSSe absorber layer and the CZTSSe TFSCs using a green synthesis process under precisely controllable vapour pressures of chalcogenide materials. The best device performance represents the CZTSSe TFSCs with the highest reported efficiency without using toxic gas and additional processes, which is certified by an external, accredited laboratory (Korea Institute of Energy Research, KIER) (ESI Table 1S and Fig. 7S). Table 1S summarizes the experimental conditions, the institutions involved, and the reported performances of CZTSSe TFSCs prepared by various deposition techniques and under different fabrication conditions. In addition, we fabricated and characterized the integrated submodule using the CZTSSe absorber layers to investigate the possibility for low cost and highly efficient CZTSSe TFSC manufacturing through a green synthesis strategy.

Experimental

The Cu-Sn-Zn stacked metallic precursor thin films were deposited on Mo coated soda lime glass substrates using the DC sputtering technique at 273 K. The precursor thin films were annealed under N_2 atmosphere to easily form the Cu-Zn and Cu-Sn alloys. To synthesize the CZTSe and CZTSSe thin films, the chalcogenide powders and precursor thin films were placed in a graphite box (406 cm^3), in a closed isothermal chamber system and heated to 540 °C for 10 min. (Fig. S1). After the annealing process, the films were naturally cooled for 1 h. The TFSCs were fabricated with a multi-layered structure of SLG/Mo/CZTSSe/CdS/i-ZnO/AZO/Al/MgF_2. The detailed experimental conditions, compositions, and chalcogenide vapor pressure of samples are listed in Table S2.

Results and discussion

Controllable $MoSe_2$ layer thickness in CZTSe thin films by adjusting Se vapour pressure

Because we adapted a closed isothermal chamber for the annealing process, it is presumably important to calculate the formation of the chalcogenide partial pressure at different temperature for different quantities of chalcogenide powders. We calculate the chalcogenide vapour pressure in the isothermal closed chamber system using the ideal gas law and the reported temperature-dependent chalcogenide vapour speciation data. Details of the pressure calculations can be found in literature.[23-26] When the temperature increases in the closed isothermal chamber, the vapour pressure of chalcogenide materials can be followed in the equilibrium vapour curve (brown line Fig. 1 (a) and dark yellow line Fig.1 (b)) until reaching the saturated pressure. The chalcogenide exists in the liquid and vapour phases below the saturated temperature (T_s) under the equilibrated system and then all of the chalcogenide liquid phase is converted into the vapour pressure at a higher temperature than T_s; then, the pressure can be calculated from the ideal gas law.[23-26] T_s is the temperature at the saturation vapour pressure

that exceeds the amount of chalcogenide placed in the annealing chamber. Fig. 1 shows the vapour pressure of Se (a) and S (b) inside of the annealing chamber with different temperature and the amount of chalcogenide powders. The different colour lines in Fig. 1 indicate the vapour pressure of chalcogenide materials in the closed isothermal chamber. The vapour pressures of chalcogenide materials can be varied by controlling the temperature and amount of the chalcogenide powders in the isothermal closed annealing system. We found that the vapour pressure of chalcogenide materials in the annealing chamber can be controlled from 5.77 to 45 Torr (Se, Fig. 1(a)) and from 11.54 to 53 Torr (S, Fig. 1(b)) under different annealing conditions.

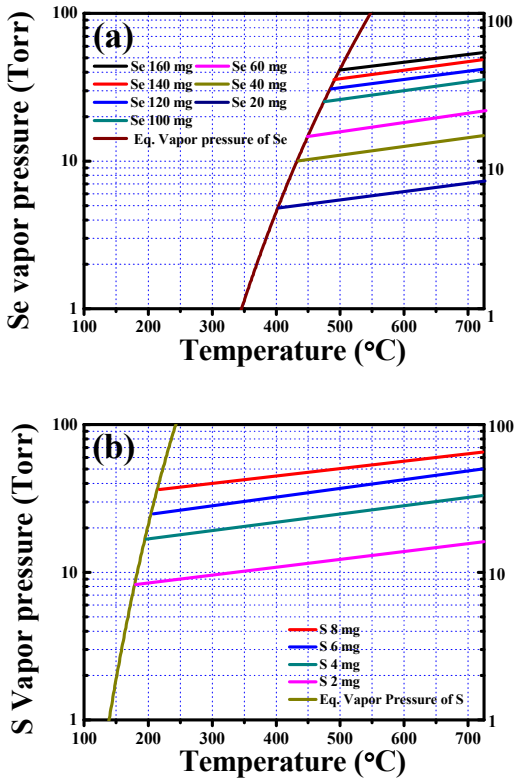

Fig. 1. Vapour pressures of Se (a) and S (b) inside of the annealing chamber with different annealing temperature and amount of S and Se powders at 406 cm^3.

The thickness of the $MoSe_2$ layer can be controlled by systematically tuning the Se partial pressure.[15] Based on the calculated Se vapour pressure (Fig.1(a)), the CZTSe thin films were prepared using different Se vapour pressures to measure the thickness of $MoSe_2$ interfacial layers. Fig. 2 shows the thickness of the $MoSe_2$ interfacial layers under different Se vapour pressures by FE-SEM characterization. The annealed thin film is not observed in the $MoSe_2$ interfacial layer at 0 Torr. The thickness of the $MoSe_2$ interfacial layers increase from 10 nm to 1.8 μm as the Se vapour pressure; however, they saturate over 35 Torr. This behaviour results from the limitation of Se diffusion in the CZTSe and $MoSe_2$ layers during the selenization process. In this case, the CZTSe thin film prepared at 5.77 Torr shows poor adhesion and uniformity at the surface. Therefore, we selected the Se vapour pressure of 11.54 Torr to improve the adhesion between the Mo and CZTSe absorber layer as well as to minimize the $MoSe_2$ interfacial layer.

Characterization of the precursor, the CZTSe thin films, and their performance in the solar cell

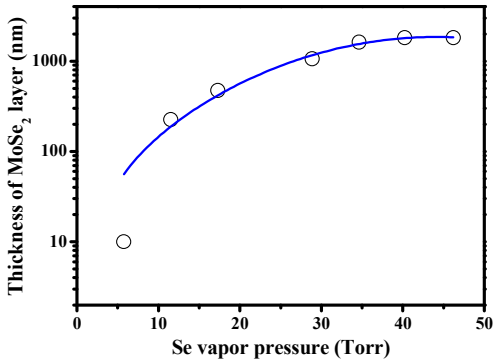

Fig. 2 Thicknesses of the $MoSe_2$ layer with different Se vapour pressures from the CZTSe thin films by selenization at 540 °C for 10 min.

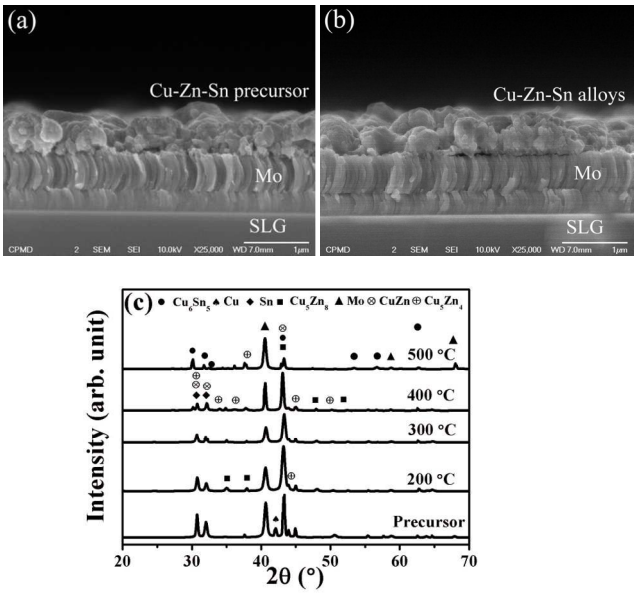

Fig. 3 FE-SEM images of (a) as-dep. and (b) annealed precursor thin films at 300 °C for 10 min. and (c) X-ray diffraction patterns of as-dep. and soft annealed samples.

The metallic precursor thin films were prepared by annealing under a N_2 atmosphere from 200 to 500 °C for 10 min. to form the Cu-Zn and Cu-Sn alloys, which act as a temporary Se diffusion barrier during selenization process and this process is called as soft-annealing process. Fig. 3 shows the FE-SEM images of (a) as-dep. and (b) annealed precursor thin films. The rough Sn layer covered by a smoother Zn and Cu layer is evident. The combined total thickness of the Cu-Zn-Sn precursor layer is

approximately 500 nm. No formation of an interfacial layer between the Mo and precursor is observed in the as-dep. and annealed thin films. The as-dep. precursor thin film shows a dense microstructure with a relatively rough morphology and, some voids located near the Mo back contact layer, and this film consists of a small size grain in the bottom region and a large grain size in the middle and top regions. However, the annealed precursor thin film prepared at 300 ºC for 10 min. (Fig. 2 (b)) shows a denser microstructure consisting of larger size grains than that without the soft-annealed process. The single peak from the metal phases (Cu and Sn) and from the Cu-based alloy phases (CuZn, Cu_5Zn_4, and Cu_5Zn_8) are observed in the as-dep. precursor thin film, while the single diffraction peaks obtained from metal phases disappeared and the Cu_6Zn_5 phase is observed after the soft-annealed process. Due to the low mutual solubility of the Sn and Zn, there is no formation of Sn-Zn alloy.[27-29] With an increase in the soft annealing temperature, the single peak from the Sn metal in the films is weakened. The compositional ratio of the as-dep. precursor and the annealed thin films indicates the Cu poor and Zn rich (Cu/(Zn+Sn)=0.66±0.05, Cu/Sn=1.96±0.1, and Zn/Sn= 1.94±1.1) conditions shown in the ESI Table S2. The precursor thin films prepared with different soft annealing temperatures were selenized at 540 ºC for 10 min. (here, Se vapour pressure is 11.54 Torr) to synthesis the kesterite CZTSe absorber layers. Fig. 2S shows the X-ray diffraction (XRD) (a) and Raman spectra (b) of CZTSe absorber layers under different soft-annealing conditions. The XRD for all of the selenized thin films shows the strong diffraction peaks located at 27 º, 45.1 º, and 53.5 º, which correspond to the (112), (204), and (312) planes for the kesterite CZTSe structure, respectively. In addition, several weak diffraction peaks are observed, regardless of the soft-annealing conditions and they have a phase pure kesterite CZTSe structure. All of the selenized thin films show a strong Raman peak located at 196 cm^{-1}, which corresponds to the kesterite structure. However, the Raman peaks from the ZnSe compounds are observed in the soft-annealed films at 400 and 500 ºC. Other weak Raman peaks correspond to the kesterite CZTSe compounds regardless of the soft-annealed conditions.

Fig.4 shows the FE-SEM images for CZTSe absorber layers without soft-annealed and with different soft-annealed temperatures. All of the annealed thin films have a dense microstructure consisting of submicron sized grains with 1.5 μm thickness and some voids between the Mo and CZTSe layers. A relatively smooth morphology is also observed, while it is rougher in the CZTSe thin film with soft-annealed at 500 ºC. Interestingly, the thicknesses of the $MoSe_2$ layers in the CZTSe thin films are dependent on the soft annealing process. The interfacial $MoSe_2$ layer of the CZTSe thin film without soft-annealed is estimated to be approximately 230 nm, which can be effectively reduced to less than 50 nm by applying the soft annealing process prior to the selenization process. The formation of dense microstructure of Cu-Zn, and the Cu-Sn alloyed layer after soft annealing preferably act as a temporary Se diffusion barrier during the selenization process, which minimizes the direct reaction of Mo with chalcogenide (Se) at high selenization temperatures. This thin interfacial $MoSe_2$ layer suggests that the series resistance (R_s) might be minimized in the solar cell device.

The CZTSe solar cells were fabricated based on samples prepared with different soft-annealed conditions and the device performances are shown in Fig. 5. Each sample contained 4-6 solar cells. The average performances, including the short circuit current density (J_{sc}), fill factor (*FF*), and efficiency (η), of the CZTSe TFSCs are improved when the soft-annealed temperatures increase to 300 ºC, and then they deteriorate when the soft-annealed temperatures further increase to 500 ºC. Interestingly, the average open circuit voltage (V_{oc}) of the CZTSe TFSCs shows the best value at a soft-annealed temperature of 200 ºC, and then it decreases with increasing soft-annealed temperatures. The CZTSe TFSC prepared at a soft-annealed temperature of 300 ºC (CZTSe-3 sample) shows the best performances; where η is 5.26 %, V_{oc} is 0.326 V, J_{sc} is 33.02 mA/cm^2, and *FF* is 49 %.

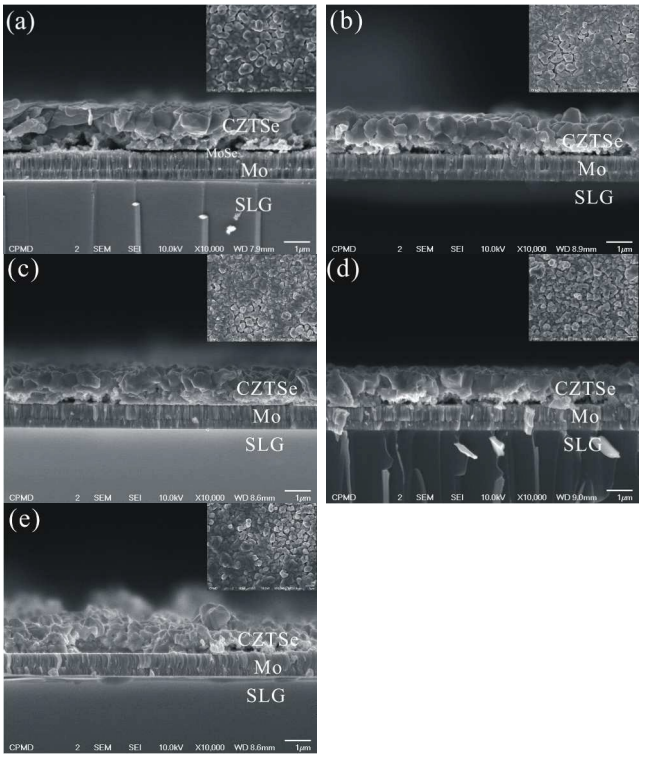

Fig.4 FE-SEM images for CZTSe absorber layers without soft- annealed and with different soft-annealed temperatures; (a) no soft annealing, (b) 200 ºC, (c) 300 ºC, (d) 400 ºC, and (e) 500 ºC.

Fig.6 shows the device parameters, including the shunt conductance (G_{sh}), ideal factor (A), reverse saturation current density (J_0), and series resistance (R_s) from the light J-V curve of CZTSe TFSCs with the best performances of samples under different soft-annealed conditions. The decreased value of A for samples prepared with soft-annealed compared with those prepared without soft-annealed leads to the reduced defect generation near the space charge region, which causes tunnelling near the space charge region and ultimately increases the carrier recombination dramatically.[3, 12] It is clearly observed in the device parameters that they are significantly improved compared with those without soft-annealed when the soft-annealed temperatures are increased to 300 ºC. The improved parameters including G_{sh} and R_s result in an improved microstructure and a reduced $MoSe_2$ thickness (Fig.4).

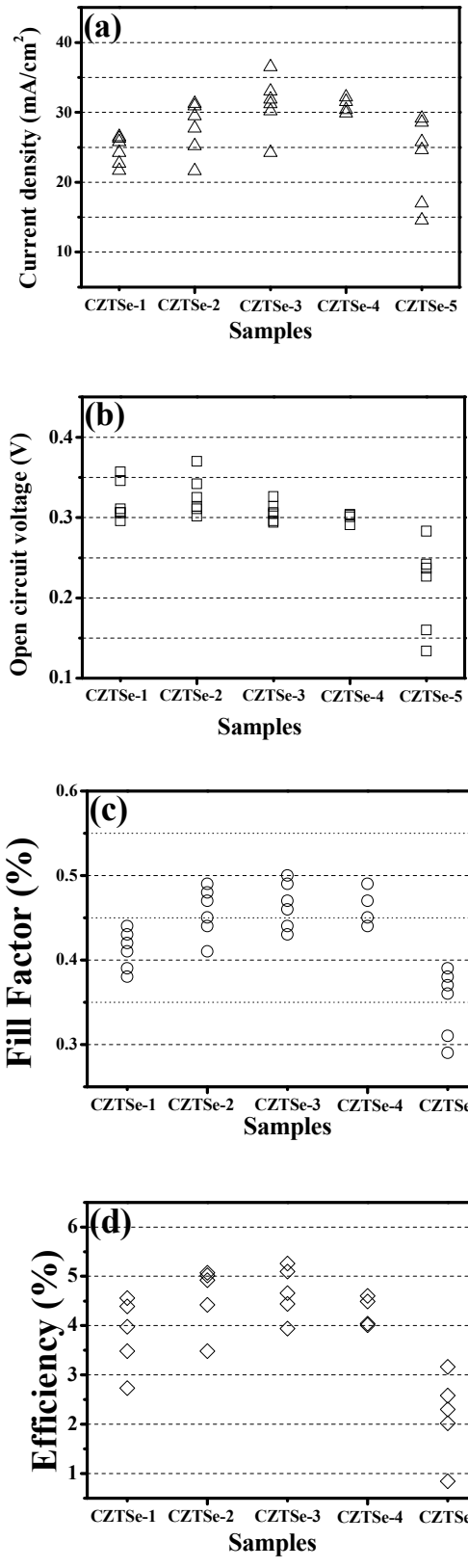

Fig.5 Device performances of the CZTSe solar cells with different soft annealed samples: (a) J_{sc}, (b) V_{oc}, (c) *FF*, and (d) η, respectively. Each sample contained 4~6 solar cells.

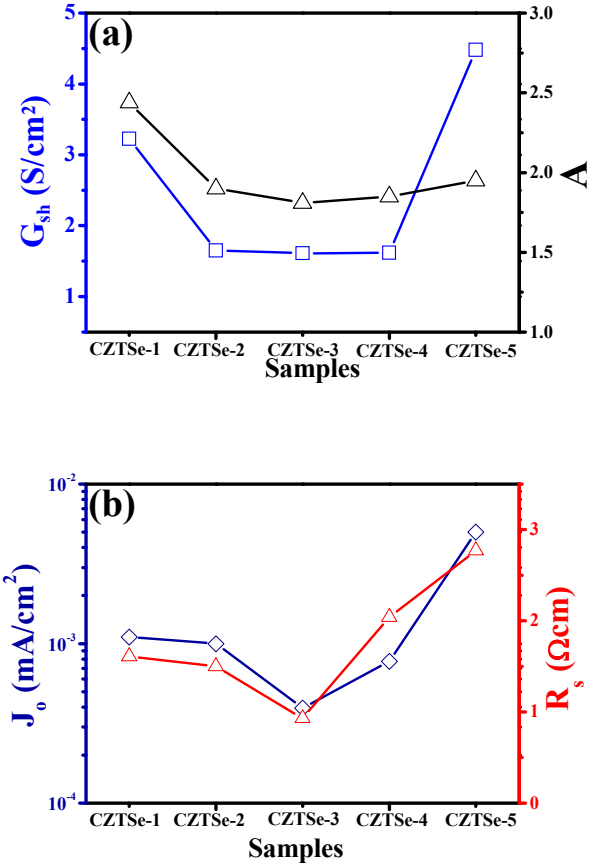

Fig.6 Device parameters from the light J-V curve of CZTSe TFSCs with different soft annealed samples: (a) G_{sh} and A (b) J_0 and R_s. These parameters were calculated from the J-V curve equation under light conditions in the SI.

The values of the device parameters of the samples deteriorate when soft-annealed temperatures are increased to 400 °C. In particular, the increase in the values of R_s, J_0, and G_{sh} at soft-annealed temperatures of 400 °C and 500 °C is attributed to the presence of ZnSe secondary phases, as shown in the Raman spectra results (ESI Fig. 2S (b)) and the rougher surface morphology (Fig. 4(e)), indicating that they may lead to increased resistivity and recombination near the space charge region in the devices.[12]

Band gap tuneable characteristics of CZTSSe thin films by adjusting the S and Se partial pressure

It is well known that the band gap energy near 1.1~1.2 eV of kesterite and CIGS TFSCs showed the best performances even though their theoretical performances were expected to achieve the best efficiency at band gap energy of 1.5 eV.[6, 9, 30] We designed the experimental conditions under different ratios of (S/(S+Se)) vapour pressures to precisely control the band gap

energy of annealed thin films, (details are shown in ESI Table 2S). Fig. 4S shows the XRD (a) and Raman spectra (b) of annealed thin films prepared under different ratios of (S/(S+Se)) vapour pressures. All of the annealed thin films show three strong diffraction peaks corresponding to the (112), (220), and (312) planes from a pure kesterite CZTS-based structure without unexpected phases. In addition, the shoulder peaks located to the right of the (112) planes are observed in the CZTSSe thin films regardless of the soft-annealed temperatures, which corresponds to the (103) plane from kesterite CZTS-based compounds. The diffraction peak positions of the (112) planes for CZTSSe thin films systemically shift toward a higher diffraction angle with increasing ratio of (S/(S+Se)) vapour pressures. Yin et al. reported the calculated equilibrium S and Se vapour pressures versus temperature for the formation reactions of Cu_2Se, $SnSe_2$, ZnSe, Cu_2SnSe_3, CZTS and CZTSe.[31] The research results and calculated vapour pressure (Fig. 1) indicated that the equilibrium pressure of S vapour is higher than that of Se over 540 °C. This thermodynamic behaviour suggests that the S atoms in the vapour easily reacted with the metallic precursor compared with that of Se at 540 °C. The composition ratios of (S/(S+Se)) in the CZTSSe thin films increase with increasing the ratio of (S/(S+Se)) vapor pressures (ESI Table 2S), which agrees well with the thermodynamic behaviour. Based on these demonstrations, the appearance of the diffraction peak shift for CZTSSe thin films can be explained by the difference in the ionic radius between S^{2-} (0.184 nm) and Se^{2-} (0.198 nm).[9] The CZTSSe thin films were characterized by Raman spectroscopy to further confirm their phase purity due to the similar crystal parameters between kesterite and the unexpected phases. The A_1 modes result from the vibrations of S or Se atoms surrounded by motionless neighbouring atoms.[25] The A_1 modes of the Raman peaks of CZTS and CZTSe compounds are observed at 338 cm^{-1} and 196 cm^{-1}, respectively. Notably, the CZTSe-3 sample show a strong Raman peak at 196 cm^{-1}, while the CZTSSe samples show a Raman peak around 200 cm^{-1}, and 330 cm^{-1} and they shift towards higher wave numbers and decreased the peak intensities. The presence of two A_1 modes for the Raman peaks from the CZTS and CZTSe compounds indicates a bi-modal behaviour and has been previously observed in intermediate compounds.[3, 32-34] No unexpected phases are observed in the CZTSSe thin films regardless of the different ratios of (S/(S+Se)) vapour pressures.

Fig. 7 shows the FE-SEM images for CZTSSe thin films prepared under different ratios of (S/(S+Se)) vapour pressures. The CZTSSe thin films show a dense microstructure with voids between the Mo and CZTSSe layers regardless of the ratios of (S/(S+Se)) vapour pressures and number of voids increase with increasing ratio of (S/(S+Se)) vapour pressures. This microstructural behaviour is attributed to the higher S vapour pressure at 540 °C (Fig.1) and it deteriorates the stability of the back contact region. Scragg et al. reported chemical insights into the instability of CZTS films during annealing, and they demonstrated the range of the S vapour pressure of decomposition for CZTS thin films during the annealing process.[18] Based on these studies, our S vapour pressures (11.54 ~ 53 Torr) might suggest the facile formation of SnS (gas phase) through the decomposition of CZTSSe near the back contact region during the annealing process, finally leading to the void formations near the back contact region and the number increases with increasing S vapour pressure. The thin $Mo(S,Se)_2$ layers below 50 nm are observed in the CZTSSe thin films, regardless of the ratio of the (S/(S+Se)) vapour pressures, indicating that the R_s could be reduced in the solar cell devices.

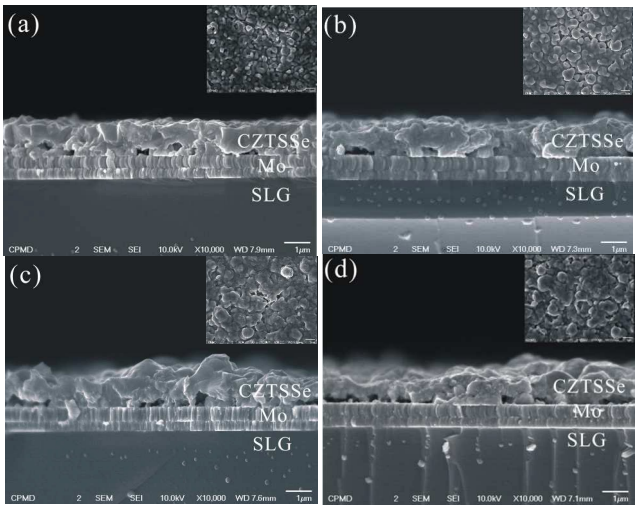

Fig. 7 FE-SEM images of CZTSSe absorber layers with different ratios of S/(S+Se) vapour pressures: (a) 0.51, (b) 0.68, (c) 0.78, and (d) 0.82.

The CZTSSe solar cells were fabricated based on samples prepared with different ratios of (S/(S+Se)) vapour pressures. Fig. 8 shows the device performances for CZTSe solar cells prepared with different ratios of (S/(S+Se)) vapour pressures. Each samples contained six solar cells. The average values of J_{sc} in the CZTSSe solar cells decrease as the ratio of (S/(S+Se)) vapour pressures increases, while those of V_{oc} show the opposite tendency. These performance behaviours are strongly related to the band gap energy of the absorber layers.[1, 2, 6, 35] The band gap energies of CZTSSe absorber layers estimated from external quantum efficiency (EQE) graphs are wider with an increasing ratio of (S/(S+Se)) vapour pressures (Fig. 5S). The absorbable wavelength of the absorber layer increases with decreasing band gap energy, and a similar tendency for kesterite solar cells has been reported by several researchers.[3, 6] The average values of *FF* and η of CZTSSe solar cells are enhanced up to a ratio of (S/(S+Se)) vapour pressure of 0.68 while those values deteriorate at a higher ratio of (S/(S+Se)) vapour pressures. The CZTSSe TFSC prepared at a ratio of (S/(S+Se)) vapour pressure of 0.68 (CZTSSe-2 sample; band gap energy of 1.1 eV) shows the best performances, with values of η : 7.01 %, V_{oc} : 0.380 V, J_{sc} : 31.45 mA/cm^2, and *FF* : 58 %. Fig.9 shows the device parameters including G_{sh}, A, J_0, and R_s from the light J-V curve of CZTSe TFSCs with the best performances under different ratios of (S/(S+Se)) vapour pressure to clearly analysis the origin of this tendency. The values of A and J_0 for CZTSSe solar cells increase with increasing ratio of (S/(S+Se)) vapour pressure. The increased values of the A and J_0 for samples are attributed to the increased S elements in the CZTSSe absorber layers. Duan et al. reported the role of S in the kesterite thin films and its effect on the defect properties. They observed a higher surface and bulk defect densities at higher S elements in the kesterite thin films

by employing admittance spectroscopy.[36] This behaviour of defect densities results in a strong recombination, even though the value of V_{oc} increased at high S content in the solar cells (Fig. 7(b)), and the overall device efficiency was reduced (Fig. 7(d)). The device parameters including G_{sh}, and R_s of CZTSSe solar cell devices indicate a similar tendency of *FF* and η. The values of G_{sh}, and R_s for samples at low S elements in the CZTSSe thin films (CZTSSe-1 and CZTSSe-2 samples) are similar to that of CZTSe-3, and those parameters at further higher S contents increase with increasing ratio of (S/(S+Se)) vapour pressure. The least favorable device parameters (G_{sh}, and R_s) resulted from increased voids between the Mo and CZTSSe layers (Fig.7).

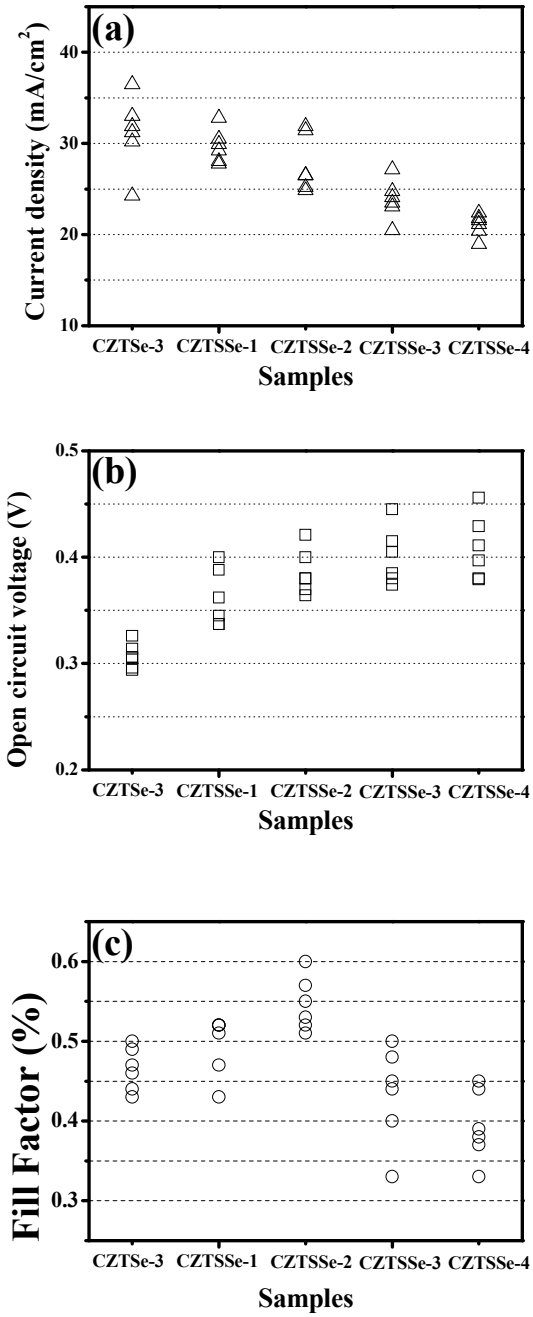

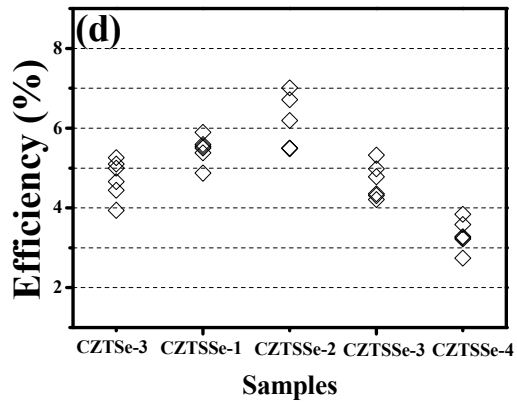

Fig. 8. Device performances of the CZTSSe solar cells with different ratios of S/(S+Se) vapor pressures: (a) J_{sc}, (b) V_{oc}, (c) *FF*, and (d) η. Each sample contained six solar cells.

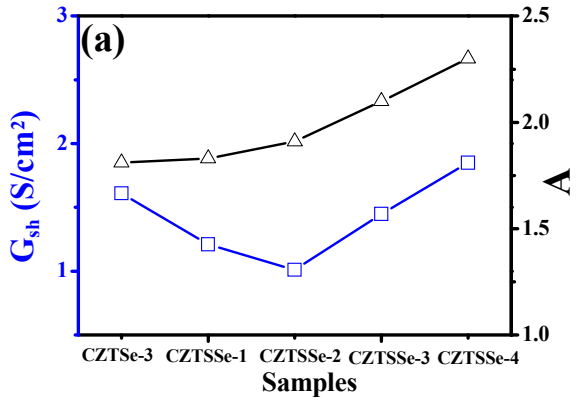

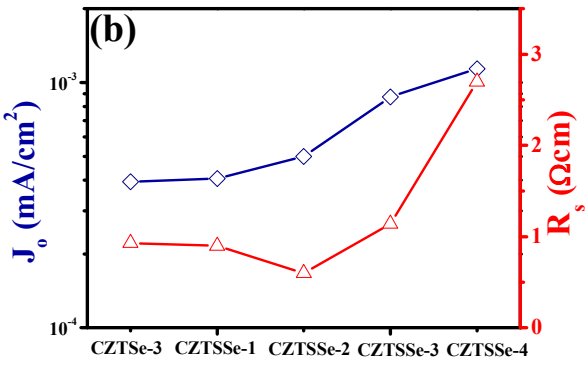

Fig. 9. Device parameters from the light J-V curve of the CZTSSe solar cells with different ratios of (S/(S+Se)) vapour pressures: (a) G_{sh} and A (b) J_0 and R_s.

Best efficiency characterization

To improve the efficiency of CZTSSe solar cells, we optimized the fabrication by controlling the ratio of the composition and (S/(S+Se)) vapour pressure in the kesterite absorber layer, the thickness and compositional ratio of the CdS buffer layer, and the thickness of the i-ZnO and AZO thin films. The optimized conditions for each layer are as follows; (i) absorber layer: Cu/(Zn+Sn) = 0.70, Zn/Sn = 1.05, and ratio of (S/(S+Se)) = 0.73; (ii) CdS layer: 65 nm; (iii) TCO layers; i-ZnO (70 nm) and AZO (380 nm); and (iv) MgF_2 layer: 150 nm. Fig. 10 shows the light J-V characteristics (a) and EQE at zero bias (b) of the best performance for CZTSSe TFSCs. The solar cell has a PEC of 9.24 % with an active area of 0.433 cm^2 under an AM 1.5 illumination. The performance characteristics of the CZTSe TFSC are as follows; V_{oc} = 454.6 mV, J_{sc} = 32.14 mA/cm^2, and FF = 63.29 %. These values were certified by KIER. To the best of our knowledge, this efficiency is one of the best cell efficiency from CZTSSe TFSC prepared via the sulfo-selenization process of a sputtered precursor without the use of toxic gas and additional processes. The EQE of the CZTSSe solar cell shows nearly 90 % in the visible region and decreases in the higher wavelength region (Fig. 10(b)), which is attributed to the short carrier diffusion length and the low minority charge carrier lifetime in the absorber layer.[3] This short carrier diffusion length is a common problem for kesterite based solar cells and it causes the high defect density in the kesterite absorber layer.[3] The optical band gap energy of the CZTSe absorber layer estimated from the EQE graph is approximately 1.1 eV. Fig. 6S shows photo (a) and cross sectional FE-SEM images for the best performance of the CZTSSe solar cell. The cross sectional FE-SEM image for the CZTSSe solar cell shows a dense microstructure consisting of submicron sized grains and many voids between the Mo and CZTSSe layers. The 40 nm thick $Mo(S,Se)_2$ layer is observed on the Mo back contact layer. The CZTSSe solar cell with best performance was used to clearly detect the element distributions and the segregation in the absorber layer near the back contact region. Fig. 11 shows the STEM images and STEM-EDS elemental mapping results for the best performance of CZTSSe TFSC. The STEM image shows that the presence of large voids (300~500 nm) is clearly observable in the bottom region of the CZTSSe absorber layer. All of the elements are well distributed in the submicron sized CZTSSe grains located at the top region of the CZTSSe absorber layer. The sharp interfacial layers are clearly observed between the CdS, TCO, and MgF_2 layers, indicating no formation of any interfacial compounds or interfacial reactions during each layer in the deposition process. In particular, the unexpected phase formations of $Zn(S,Se)_x$ and SnO_x between the CZTSSe absorber and the Mo back contact layers are clearly observed.

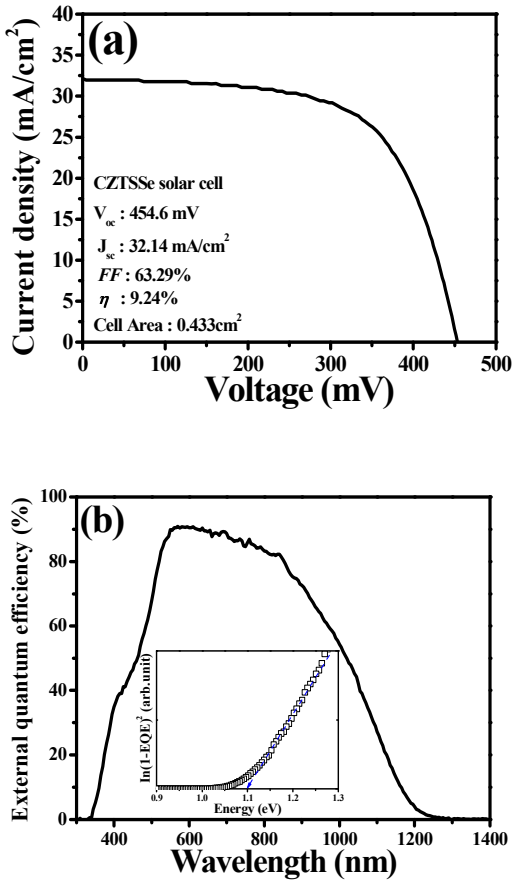

Fig.10 J-V (a) and EQE (b) of best efficient CZTSSe TFSC. The insert is a plot of $(\ln(1\text{-EQE}))^2$ versus energy, which is used to determine the band gap energy of the absorber layer.

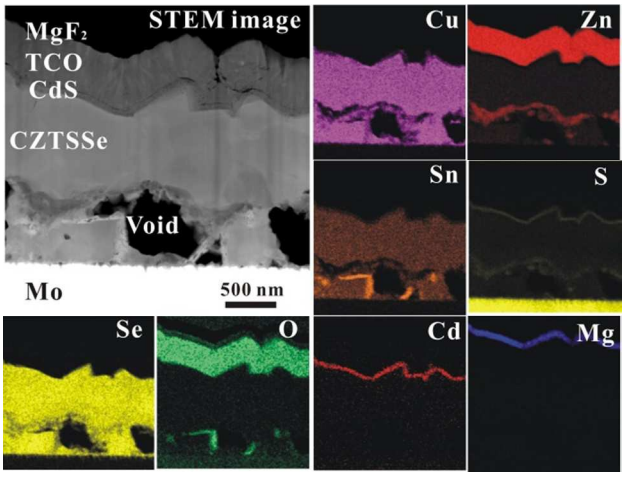

Fig.11 STEM image and STEM-EDS elemental mapping results for best efficient CZTSSe TFSC.

Discussion

(i) Comparative study of the IBM cell

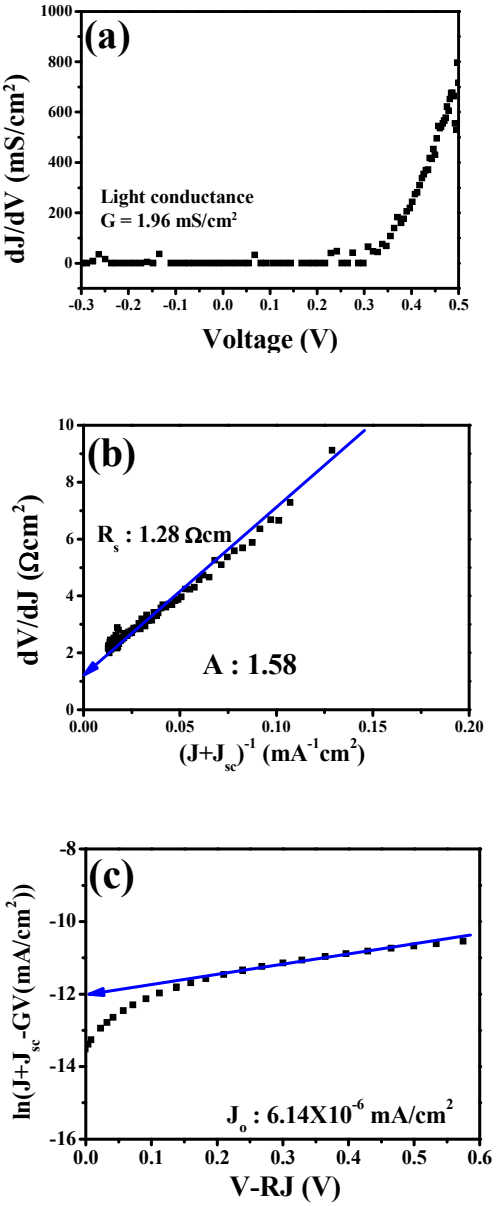

Fig.12 Plots of d*J*/d*V vs V* (a), d*V*/d*J* vs $(J+J_{sc})^{-1}$ (b), and ln($J+J_{sc}$-*GV* vs *V-RJ*) (c) redrawn from the light *J-V* curves of the best efficient CZTSSe solar cell.

To understand the lower performance of the CZTSSe solar cell compared with the highest efficiency IBM device prepared using a hydrazine based solution process, the performances and parameters for the best efficient CZTSSe solar cell and the previously reported IBM cell are summarized in Table 1. The solar cell parameters were obtained and are shown in Fig. 12. Fig. 12 shows the dJ/dV vs, V curve (a), dV/dJ vs, $(J+J_L)$ curve (b), and log scale ($J+J_{sc}$-GV) vs (V-RJ) (c) of the CZTSe TFSC under light conditions from a one-diode model (ESI Eq. (1S) and (2S)). The different performance of V_{oc} and *FF* is clearly observed between the present results and the IBM cells. In addition, all of the device parameters including G_{sh}, A, J_0, and R_s for the present results are higher than are those of IBM cell. The V_{oc}-deficit characteristic, obtained from the difference between the band gap energy and the V_{oc} of the present cell (685 mV), is worse than that of the IBM cell (617 mV) (Table 1). The V_{oc}-deficit characteristics are attributed to a high recombination rate in the buffer/absorber interface and a low minority charge carrier lifetime, as reported in earlier CIGS- and CZTS-based TFSCs studies.[35] The higher values of A (1.58) and J_0 (6.14×10^{-6} mA/cm^2) for the present results compared with that of the IBM cell (A; 1.45 and J_0; 7.0×10^{-8} mA/cm^2) imply a higher recombination rate in the buffer/absorber interface. Finally, the V_{oc} for the present result shows a lower value, even though they have similar optical band gap energies (Table 1).[3] These higher recombination rate behaviours provide evidence for higher defect concentrations in the absorber surface region for the present cell than that of IBM cell.[6] In addition, the lower value of *FF* for the present results than that of IBM is strongly related to the parameters including J_0, A, and R_s. In particular, the value of R_s (1.28 Ωcm^2) in the present cell is approximately two times higher than that of the IBM cell (0.72 Ωcm^2). The higher R_s in the present cell could explain the unexpected phase formations of $Zn(S,Se)_x$ and the amorphous like SnO_x near the bottom region of the CZTSSe absorber layer (Fig. 11). The XRD and Raman spectra results for the CZTSSe absorber thin film do not detect $Zn(S,Se)_x$ and SnO_x (ESI Fig. 4S). Recently, Sardashti et al. reported the formation of grain boundaries surrounded by SnO_x for high efficient CZTSSe solar cell with a 12.6 % efficiency using a highly surface-sensitive Auger Nano probe elemental mapping characterization, which acts as a unique effective passivation that limits electron-hole recombination.[37] In the case of the present results, the location of SnO_x is near voids in the bottom region of the CZTSSe absorber layer, and it does not play a role in passivation for recombination in the grain boundaries, but it increases the R_s in the solar cell device due to the higher resistivity of amorphous like SnO_x. In addition, the $Zn(S,Se)_x$ phase has a high resistivity leading to an increased R_s in the solar cell device. The value of G_{sh} in the present cell is 1.96 mS/cm^2, which is higher than that of the IBM cell (1.61 mS/cm^2) as presented in Table 1. This higher value of G_{sh} in the present cell might explain the presence of unexpected secondary phases and many voids near the bottom region, which leads to the reduced J_{sc} value in the present device. Based on these discussions for comparative studies, we conclude that the solar cell parameters of the present device are worse than those of the IBM cell because of the presence of voids, unexpected phases including $Zn(S,Se)_x$ and SnO_x, and the high defect density of the absorber layer. These factors lead to a higher recombination rate at the interface between CdS/CZTSSe absorber (resulting in the increase in A, G_{sh}, and J_0) and higher R_s than those of the IBM cell. It is thought that the efficiency of our CZTSSe cell can be improved by removing the voids and unexpected phases near the back contact.

(ii) Applicability of CZTSSe submodules.

The CZTSSe submodule was fabricated and characterized to investigate the possibility for low cost and highly efficient CZTSSe TFSC manufacturing using a green synthesis strategy. The CZTSSe submodules were fabricated using a commonly integrated process that employs 3-step patterning methods. The detailed fabrication process of the CZTSSe submodule is described in the experimental part for ESI and ESI Fig. 8S. The CZTSSe submodule monolithically integrated eight cells (active area: 22.4 cm^2). Using this fabrication process, we achieved 2.76 % efficiency (V_{oc}: 3.74 V, J_{sc}: 40.31 mA/cm^2, and *FF*: 42 %). The performance of submodule solar cells were improved until 8 solar cells, while further they were dramatically worse further night interconnected solar cell due to the poor fill factor. The poor performance of the CZTSSe submodule is attributed to the low *FF* resulting from high R_s, low R_{sh}, which are resulted from the mechanical patterning technique (P2 and P3). They could create a large dead area in the submodule. Although the CZTSSe submodule indicates poor performances, this research could introduce a pathway to green fabrication in the low cost and highly efficient TFSC industrialization. Studies on optimizing the precise control of the compositional ratio in the CZTSSe absorber layer, deposition conditions for each layer, and changing from mechanical patterning to laser pattering (P2 and P3) are currently progress.

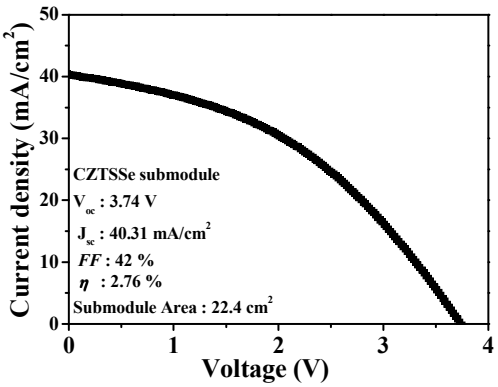

Fig. 13 J-V graph for the CZTSSe submodule with the best efficiency.

Conclusions

In summary, a 9.24 % efficient CZTSSe TFSC was successfully fabricated by a non-toxic, short, and simple sulfo-selenization process of Cu/Sn/Zn metal stacked precursor thin films without using toxic H_2S gas, even though the CZTSSe layer has a relatively thin thickness (1 μm), unexpected phases including $Zn(S,Se)_x$ and amorphous like SnO_x, and many voids near the back contact region. The device parameters for the present cells are poor compared with those of the IBM cell due to the higher recombination rate at the interface between the CdS/CZTSSe absorber and the higher R_s in the solar cell. Our best performance exhibited an efficiency of 9.24 %, which is the highest efficiency reported for pure CZTSSe TFSCs prepared by the sulfo-selenization of a sputtered precursor without the use of toxic gas and additional processes. We are underdoing the development and application of Cd-free buffer layer prepared by chemical bath deposition and atomic layer deposition techniques to balance the toxicity with high performance. We also achieved 2.76 % efficient CZTSSe submodule by monolithically integrating eight cells (active area: 22.4 cm^2). The performance of the CZTSSe solar cell and the submodule could be improved by an additional optimization process, including removal of voids and unexpected phases, and using a thicker absorber layer. This research presents a good possibility for the development of non-toxic, highly efficient and cost effective CZTSe TFSCs for the industrialization field.

Table 1. Device characterization and comparison with the best reported CZTSSe devices using the sputtering technique.[a] Light shunt conductance (G), series resistance (Rs), ideal factor (A), and reverse saturation current density (J_0) were calculated from J-V curve under the light conditions (ESI Eq. 1S and 2S). [b] All of the parameters are taken from the hydrazine based CZTSSe thin film solar cells reported by IBM researchers [38]

Method	Institute	J_{sc} (mA/cm^2)	V_{oc} (mV)	FF (%)	η	Eg (eV)	Eg (eV)/q-V_{oc} (mV)	G_{SL}[a] (mS/cm^2)	R_s[a] (Ωcm^2)	A[a]	J_o (mA/cm^2)[a]	Ref.
Sputtering (Se vapor)	**CNU**	**32.14**	**454.6**	**63.29**	**9.24**	**1.10**	**685**	**1.96**	**1.28**	**1.58**	**6.14 ×10^{-6}**	**This work**
Solution (Hydrazine, Se vapor)[b]	**IBM**	**35.2**	**513.4**	**69.8**	**12.6**	**1.13**	**617**	**1.61**	**0.72**	**1.45**	**7.0 ×10^{-8}**	**[38]**

Journal Name

ARTICLE

ASSOCIATED CONTENT

Supporting Information. Experimental methods and additional characterization data.

AUTHOR INFORMATION

Corresponding Author

**** Jin Hyeok. Kim:** Email: jinhyeok@chonnam.ac.kr,TEL : 82-62-530-1709**,** FAX: 82-62-530-1699

*** Jeong Yong. Lee:** Email:j.y.lee@kaist.ac.kr,TEL : 82-42-350-4216, FAX: 82-42-350-3310

ACKNOWLEDGMENT : This work is supported by the Human Resources Development (No. 20124010203180) of the Korea Institute of Energy Technology Evaluation and Planning (KETEP) grant funded by the Korea government Ministry of Trade, Industry and Energy.

References

1. A. Polizzotti, I. L. Repins, R. Noufi, S.-H. Wei and D. B. Mitzi, *Energy Environ. Sci.*, 2013, **6**, 3171-3182.
2. M. Johnson, S. V. Baryshev, E. Thimsen, M. Manno, X. Zhang, I. V. Veryovkin, C. Leighton and E. S. Aydil, *Energy Environ. Sci.*, 2014, **7**, 1931-1938.
3. D. B. Mitzi, O. Gunawan, T. K. Todorov, K. Wang and S. Guha, *Sol. Energy Mater. Sol. Cells*, 2011, **95**, 1421-1436.
4. J. Kim, H. Hiroi, T. K. Todorov, O. Gunawan, M. Kuwahara, T. Gokmen, D. Nair, M. Hopstaken, B. Shin, Y. S. Lee, W. Wang, H. Sugimoto and D. B. Mitzi, *Adv. Mater.*, 2014, **26**, 7427-7431.
5. P. Jackson, D. Hariskos, R. Wuerz, O. Kiowski, A. Bauer, T. M. Friedlmeier and M. Powalla, *phys. stat. sol. (RRL) Rap. Res. Lett.*, 2015, **9**, 28-31.
6. M. T. Winkler, W. Wang, O. Gunawan, H. J. Hovel, T. K. Todorov and D. B. Mitzi, *Energy Environ. Sci.*, 2014, **7**, 1029-1036.
7. S. W. Shin, J. H. Han, C. Y. Park, A. V. Moholkar, J. Y. Lee and J. H. Kim, *J. Alloys Compd.*, 2012, **516**, 96-101.
8. S. W. Shin, S. M. Pawar, C. Y. Park, J. H. Yun, J.-H. Moon, J. H. Kim and J. Y. Lee, *Sol. Energy Mater. Sol. Cells*, 2011, **95**, 3202-3206.
9. S. W. Shin, J. H. Han, Y. C. Park, G. L. Agawane, C. H. Jeong, J. H. Yun, A. V. Moholkar, J. Y. Lee and J. H. Kim, *J. Mater. Chem.*, 2012, **22**, 21727-21732.
10. B. Shin, Y. Zhu, N. A. Bojarczuk, S. Jay Chey and S. Guha, *Appl. Phys. Lett.*, 2012, **101**, 053903.
11. B. Shin, O. Gunawan, Y. Zhu, N. A. Bojarczuk, S. J. Chey and S. Guha, *Prog. Photovolt.: Res. Appl.*, 2011, **21**, 72-76.
12. I. Repins, C. Beall, N. Vora, C. DeHart, D. Kuciauskas, P. Dippo, B. To, J. Mann, W.C. Hsu, A. Goodrich and R. Noufi, *Sol. Energy Mater. Sol. Cells*, 2012, **101**, 154-159.
13. Y. S. Lee, T. Gershon, O. Gunawan, T. K. Todorov, T. Gokmen, Y. Virgus and S. Guha, *Adv. Energy Mater.*, 2014, **5**, 1401372.
14. G. Brammertz, M. Buffière, S. Oueslati, H. ElAnzeery, K. Ben Messaoud, S. Sahayaraj, C. Köble, M. Meuris and J. Poortmans, *Appl. Phys. Lett.*, 2013, **103**, 163904.
15. B. Shin, N. A. Bojarczuk and S. Guha, *Appl. Phys. Lett.*, 2013, **102**, 091907
16. J. J. Scragg, T. Kubart, J. T. Wätjen, T. Ericson, M. K. Linnarsson and C. Platzer-Björkman, *Chem. Mat.*, 2013, **25**, 3162-3171.
17. J. J. Scragg, J. T. Wätjen, M. Edoff, T. Ericson, T. Kubart and C. Platzer-Björkman, *J. Am. Chem. Soc.*, 2012, **134**, 19330-19333.
18. H. Cui, X. Liu, F. Liu, X. Hao, N. Song and C. Yan, *Appl. Phys. Lett.*, 2014, **104**, 041115.
19. S. Lopez-Marino, M. Placidi, A. Perez-Tomas, J. Llobet, V. Izquierdo-Roca, X. Fontane, A. Fairbrother, M. Espindola-Rodriguez, D. Sylla, A. Perez-Rodriguez and E. Saucedo, *J. Mater. Chem. A*, 2013, **1**, 8338-8343.
20. F. Liu, K. Sun, W. Li, C. Yan, H. Cui, L. Jiang, X. Hao and M. A. Green, *Appl. Phys. Lett.*, 2014, **104**, 051105.
21. J. Li, Y. Zhang, W. Zhao, D. Nam, H. Cheong, L. Wu, Z. Zhou and Y. Sun, *Adv. Energy Mater.*, 2015,**5**, 1402178.
22. J. J. Scragg, T. Ericson, T. Kubart, M. Edoff and C. Platzer-Björkman, *Chem. Mat.*, 2011, **23**, 4625-4633.
23. E. H. Baker, *J. Chem. Soc. A: Inorg., Physical, Theo.*, 1968, 1089-1092.
24. H. Rau, T. R. N. Kutty and J. R. F. Guedes De Carvalho, *J. Chem.Therm.*, 1973, **5**, 833-844.
25. H. Rau, *J. Chem. Therm.*, 1974, **6**, 525-535.
26. D.Y. Peng and J. Zhao, *J. Chem. Thermo.*, 2001, **33**, 1121-1131.
27. J. J. Scragg, D. M. Berg and P. J. Dale, *J. Electroanal. Chem.*, 2010, **646**, 52-59.
28. J. J. Scragg, P. J. Dale and L. M. Peter, *Electrochemistry Communications*, 2008, **10**, 639-642.
29. J. J. Scragg, P. J. Dale and L. M. Peter, *Thin Solid Films*, 2009, **517**, 2481-2484.
30. S. W. Shin, I. Y. Kim, K. V. Gurav, C. H. Jeong, J. H. Yun, P. S. Patil, J. Y. Lee and J. H. Kim, *Curr. Appl. Phys.*, 2013, **13**, 1837-1843.
31. X. Yin, C. Tang, L. Sun, Z. Shen and H. Gong, *Chem. Mat.*, 2014, **26**, 2005-2014.
32. I. V. Bodnar', *Semicond.*, 1997, **31**, 41-43.
33. L. Grenet, S. Bernardi, D. Kohen, C. Lepoittevin, S. Noël, N. Karst, A. Brioude, S. Perraud and H. Mariette, *Sol. Energy Mater. Sol. Cells*, 2012, **101**, 11-14.
34. A. G. Kontos, Y. S. Raptis, M. Straßburg, U. W. Pohl and D. Bimberg, *Thin Solid Films*, 2003, **428**, 185-189.
35. U. Ghorpade, M. Suryawanshi, S. W. Shin, K. Gurav, P. Patil, S. Pawar, C. W. Hong, J. H. Kim and S. Kolekar, *Chem. Commun.*, 2014, **50**, 11258-11273.

36. H.S. Duan, W. Yang, B. Bob, C.-J. Hsu, B. Lei and Y. Yang, *Adv. Funct. Mater.*, 2013, **23**, 1466-1471.
37. K. Sardashti, R. Haight, T. Gokmen, W. Wang, L.-Y. Chang, D. B. Mitzi and A. C. Kummel, *Adv. Energy Mater.*, 2015, **5**,1402180.
38. W. Wang, M. T. Winkler, O. Gunawan, T. Gokmen, T. K. Todorov, Y. Zhu and D. B. Mitzi, *Adv. Energy Mater.*, 2013, **4**,1301465.